www.pnas.org

Supplementary Information for
Inertially enhanced mass transport using 3D-printed porous flow-through electrodes with periodic lattice structure

Victor A. Beck, Anna N. Ivanovskaya, Swetha Chandrasekaran, Jean-Baptiste Forien, Sarah E. Baker, Eric B. Duoss, and Marcus A. Worsley

Victor A. Beck, Anna N. Ivanovskaya, Marcus A. Worsley
Email:beck33@llnl.gov, ivanonvskaya1@llnl.gov, worlsey1@llnl.gov

This PDF file includes:

Supplementary text
Figures S1 to S9
SI References

Supporting Information Text

Experimental procedures

Ink preparation and 3D printing of flow through electrodes. The electrodes for flow tests involve preparation of a carbon ink, 3D printing of the ink and finally carbonizing them to obtain 3D printed electrodes. The carbon ink used in this study is a graphene oxide-based ink, which after processing yields 3D graphene aerogel (GA) electrodes. Single layer graphene oxide sheets (GO) having a lateral dimension of 300-800 nm purchased from Cheaptubes Inc. were used to prepare the aerogel inks. The GO suspension was prepared by ultra-sonicating 0.8 g of GO in 20 g of water for 24 h in a sonication bath which is maintained at a constant temperature of 12°C to avoid heating during the process. This combination yields a GO concentration of 40 mg/ml. The suspension is then mixed with 5 wt% of hydroxypropyl methylcellulose GO-ink in a planetary Thinky mixer at 2000 rpm for 5 minutes. To add stiffness and stability to the ink, chopped carbon fibers with water compatible sizing is added to ink at 25mg/ml concentration. Addition of stiff particles, carbon fibers in this case, restricts volume shrinkage of graphene oxide aerogels during the high-temperature carbonization process.

The ink was loaded into a 10ml syringe barrel (EFD) and centrifuged for a minute at 4500 rpm to remove air bubbles, after which the ink was extruded through a micro nozzle (400 μm diameter) to pattern 3D structures on a glass substrate. For direct ink writing (DIW), the syringe was attached by a luer-lock to a smooth-flow tapered nozzle whose inner diameter(d) is 400 μm. The ink was then extruded by means of an air powered fluid dispenser (Ultimus V, EFD) which provides an appropriate pressure (in the range of 15-20 psi) for writing and the writing speed was kept at 5 mm/sec for all the 3D printed structures. Although it is not mandatory to change the PTFE nozzle tip between the prints, for the fabrication of electrodes, a new tip was used for every sample. SC lattices with multiple orthogonal layers of parallel cylindrical rods were printed alternately. The diameter of the cylindrical rods equals the diameter of nozzle and the center-to-center rod spacing of 800 μm (for 400 μm nozzle). The height of the electrodes was kept constant at 2.16 mm so that each print had a total of 9 layers and the layers were stacked on the structure such that each layer has a y spacing 240 μm. For FCC lattices, an off set of 400 μm was given in both x and z directions, and the center-to-center rod spacing was set at 800 μm (for 400 μm nozzle) so that every odd layer will cover the gap in the even layers. Like SC lattices, the total number of layers is fixed to 9.

To avoid cracking or drying due to evaporation of water, soon after printing, the 3D printed structures are immersed in liquid nitrogen and freeze dried for 48 h in vacuum to form aerogels. The average density of as-dried electrodes was 51 ± 4 mg/cm^3 for SC and 49 ± 5 mg/cm^3 for FCC respectively. The printed aerogels are then subjected to a heat treatment process where the samples were heated in a tube furnace under nitrogen atmosphere at 1050°C for 3 h with a heating and cooling rate of 2°C/min to form graphene aerogels (GA). After carbonization, the average densities of electrodes were 32 ± 4 mg/cm^3 for SC and 30 ± 2 mg/cm^3 for FCC.

The surface area of the GA aerogel ink was determined by Brunauer-Emmett-Teller (BET) method using an ASAP 2020 Surface Area Analyzer (Micromeritics Instrument Corporation) via nitrogen porosimetry (1). Samples of approximately 0.1 g were heated to 573 K under vacuum (10-3 Pa) for at least 24 hours to remove all adsorbed species. The measured surface area of the aerogel was 4.7 m^2/g. We 3D printed a monolith using the GA ink and post-processed in a similar way as the 3D FTEs, and the density of the aerogel was measured to be 43.25 mg/cm^3.

Numerical methods. High resolution, continuum, computational fluid dynamics is used to simulate the flow and mass transport in the lattice geometries and enable direct comparison to the experimentally studied systems. At the limiting current, the surface concentration of the lone reactive species (i.e., $Fe(CN)_6^{4-}$ for oxidation of ferrocyanide) is zero and the electrochemical and electrostatic problems are decoupled (2). The complete, steady mass transport behavior can be described by two, one-way coupled partial differential equations for the fluid flow field, $\vec{v}$, and species concentration, c as shown in Eq. 6 and Eq. 7 in the main text.

We set an inlet concentration, $c_b = [Fe(CN)_6^{4-}]_{Inlet}$, and inlet flow velocity on the boundary upstream of the electrode, U, equal to the superficial velocity. Because the intrinsic area per volume of the fiber is extremely high and the permeability is very low, no flow penetrates into the fiber and the reaction is concentrated near the fiber surface. Thus, in the simulation the fibers are treated as solids. On the fiber surface the concentration is fixed to zero (i.e., limiting current conditions(2)), and the fluid obeys the no-slip boundary condition. At outlet and symmetry boundaries homogeneous Neumann (no flux) boundary conditions are applied. Simulations are performed in the computational domains pictured in Figure 1C at the same flow rates as the experiment. In Figure S5 the detailed procedure for creating the simulation domain, the location of the boundary conditions, and the location of the print planes is presented.

We use the commercial software tool Starccm+ (Siemens) to solve Eq. 6 and Eq. 7 subject to the continuity equation. The simulated domains are pictured in Figure 1C and again in Figure S5 and Figure S6A. These correspond to idealizations of the printed structures used in the experiments. Layers are spaced $0.4325 d_f$, and within the layer the pitch from fiber center to fiber center in both in-plane directions (perpendicular to the flow direction) is set to 1.925 d_f. The symmetric domain and assumed steady flow allow us to use an extracted periodic unit cell as shown in Figure S5 and Figure S6A. As pictured in Figure S6A, we use the built-in meshing tools to generate a predominantly hexahedral (Trimmer) computational mesh with finite-volume, cell size of d_f /160. To resolve the transport behavior in the boundary layers, the mesh is augmented with surface parallel, prism layers of thickness (d_f /50) adjacent to the fiber surfaces and composed of 16 cells with a stretching ratio of 1.1. The smallest cell is adjacent to the fiber and has thickness $\approx d_f$ /1855.

For the simulations in the manuscript, we change the inlet velocity boundary condition to correspond to the experimentally measured velocities. Thus, though we explore a range of Pe_f and Re_f, these are not independently varied. Further, we performed time-dependent simulation on a full periodic domain at the highest Re_f reported in the manuscript and found that the flow remained steady with the exception of the FCC simulation at $Re_f = 60.76$. Computations were performed on Livermore Computing cluster resources with each simulation run requiring 1-2K core-hour to converge to a solution.

Lastly, though not analyzed nor experimentally measured in the main text, we used the simulation to determine the low Re permeability to be 1.5×10^{-9} for the SC electrodes and 1.3×10^{-10} for the FCC.

Relationship between local and overall mass transfer coefficients. In Eq. 1 of the main text we define a local mass transfer coefficient at downstream position, x,

$$k_m(x) \equiv \frac{\langle c \rangle_v}{\left\langle -D_0 \vec{n} \cdot \vec{\nabla} c \right\rangle_s} \qquad [1]$$

As described in Figure S8, $\langle * \rangle_v$ is the velocity weighted average concentration in planes perpendicular to the flow direction (i.e., y,z directions) and $\langle * \rangle_s$ is the surface average along the intersection of the plane and fiber surface. Thus, in the absence of dispersion, the cross-stream averaged species conservation equation is,

$$U \frac{d \langle c \rangle_v}{dx} = -k_m a \langle c \rangle_v \qquad [2]$$

where we introduce the fiber surface area (A_E) per volume (V_E) assuming solid fibers and $a \equiv A_E / V_E$. This can be integrated over the length of the electrode L and rearranged to determine the volumetrically averaged mass transfer coefficient (3–5):

$$k_m a = -\frac{U}{L} \log\left(1 - \frac{I_{lim}}{nFQc_b}\right) \qquad [3]$$

where I_{lim} is the limiting current, n is the number of electrons transferred in the reaction, F is Faraday's constant, and Q is the imposed flow rate (i.e., Q = superficial velocity * frontal area = $U * A$). In the high flow-rate/low-conversion limit the concentration throughout the electrode approaches the bulk concentration and,

$$\langle k_m a \rangle \equiv \lim_{\langle c \rangle_v \to c_b} \langle k_m a \rangle_L = \frac{I_{lim}}{nFV_E c_b} \qquad [4]$$

which agrees with typical definitions of the volumetrically averaged product of the mass transfer coefficient and the internal electrode area (6). We note that in this limit, the volumetrically averaged mass transfer coefficient is equal to the length averaged local mass transfer coefficient defined in Eq. 1. In the main text, we define $k_m a \equiv \langle k_m a \rangle_L$.

Justification for neglecting electroosmotic flow. Our analysis and simulations did not model electroosmotic flow in the electrode. The Debye length for the 1M KCl solution is calculated using (7),

$$\lambda_D = \sqrt{\frac{\epsilon_w RT}{2F^2 c^\infty}}, \qquad [5]$$

where $T = 300$K is the temperature, R is universal gas constant, $\epsilon_w = 7.1 \times 10^{-10}$ F/m is the permittivity of water, and $c^\infty = 1$M is the concentration of the electrolyte. This yields $\lambda_D \approx 0.3$nm and is several orders of magnitude smaller than the 400 μm diameter filaments studied in the manuscript. The double layer is thus negligibly thin compared to the geometric, concentration boundary layer, and flow scales.

The expected flow velocity induced by electroosmosis can be calculated from the Helmholtz-Smoluchowski formula,

$$\vec{u}_{eo} = -\frac{\epsilon_w \zeta}{\mu} \vec{E}, \qquad [6]$$

where μ is the fluid viscosity, $\vec{E}$ is the electric field parallel to the surface, and ζ is the zeta potential at the electrolyte-filament boundary. We did not directly compute nor measure the zeta potential in the system. However, we can still provide an upper-bound on the magnitude of the expected electroosmotic flow. In our experiments, the largest voltage measured between the working and reference electrode was $\Delta\Phi = 1.2$ V. This serves as an upper-bound on the zeta potential. Further, we can provide an upper bound on the electric field by assuming that this same potential drop occurs over the thickness of the electrode (in practice these will not have the same value, but the potential difference serves merely as a bound). Thus,

$$|\vec{u}_{eo}| < \frac{\epsilon_w \Delta\Phi^2}{\mu L}. \qquad [7]$$

Substituting into this expression yields $|\vec{u}_{eo}| < 7.6 \times 10^{-4}$ cm/s which is 10x smaller than the average flow velocity in the voids between the filaments at the *lowest* flow rate used in the manuscript. The actual zeta potential will likely be at least an order of magnitude smaller (8) and the electric field magnitude will also be significantly smaller since it is predominantly directed *into* the filaments and not parallel to the filament-electrolyte interface. We thus neglect the impact of electroosmosis in our system.

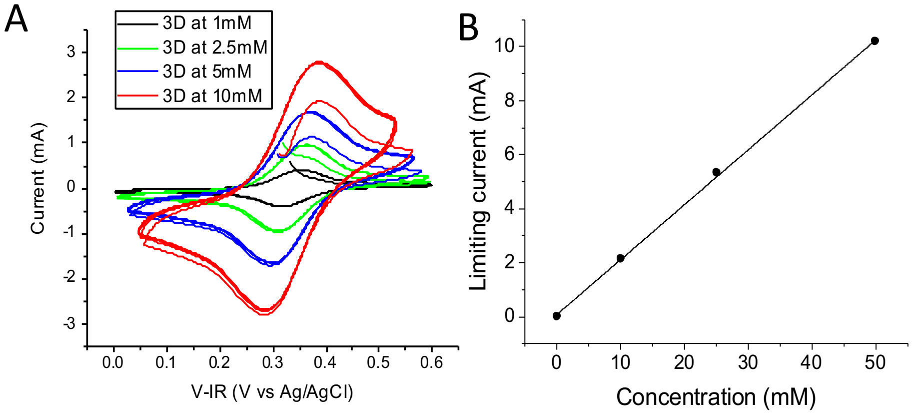

Fig. S1. (A) Cyclic voltammetry curves under no flow conditions at various concentrations of Potassium hexacyanoferrate (II) in 1M KCl measure on 3D printed graphene electrode with SC structure. (B) Limiting currents as a function of Potassium hexacyanoferrate (II) concentration in 1M KCl measured with through 3D-printed graphene electrode with SC geometry under flow rate 3 ml/min.

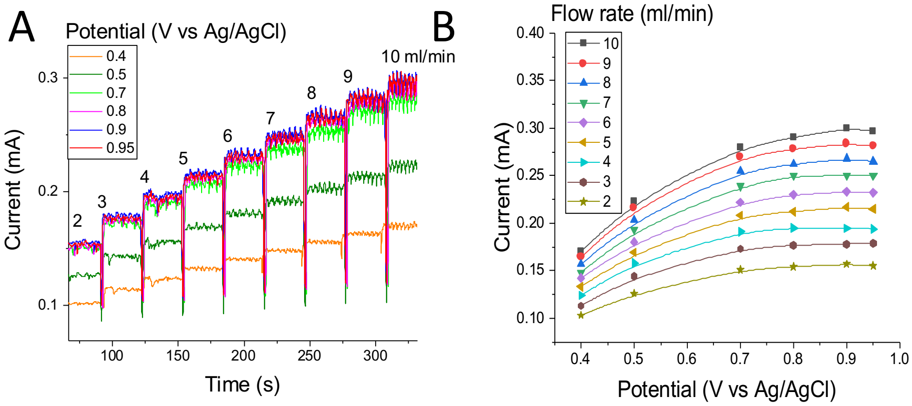

Fig. S2. (A) Chronoamperometry curves measured while flowing Potassium hexacyanoferrate (II) (1mM solution in 1M KCl) at various flow rates through a 3D-printed graphene electrode with SC geometry held at a fixed potential; (B) Steady state voltammetry curves reconstructed from chronoamperometry.

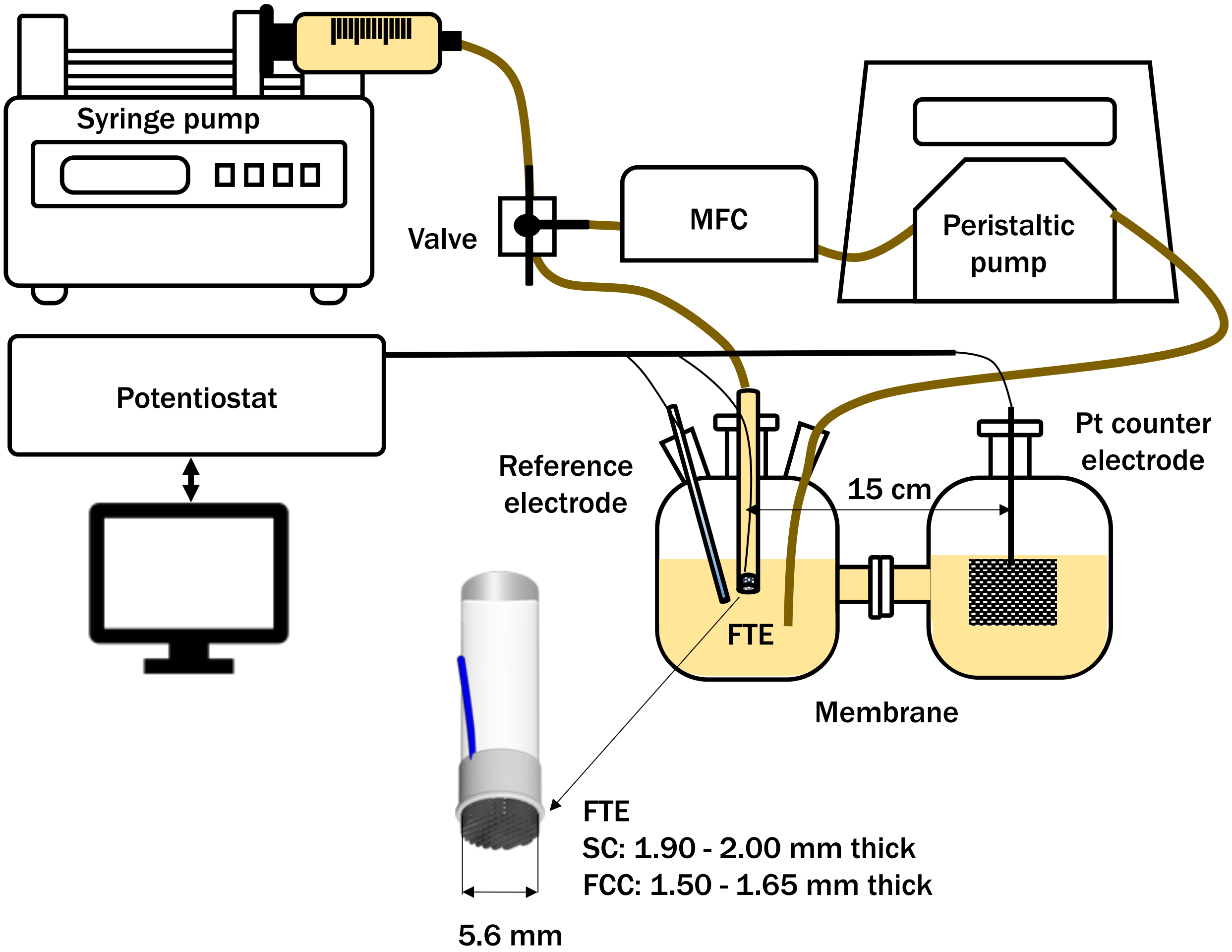

Fig. S3. Schematic of experimental setup for measuring limiting currents as a function of flow rate.

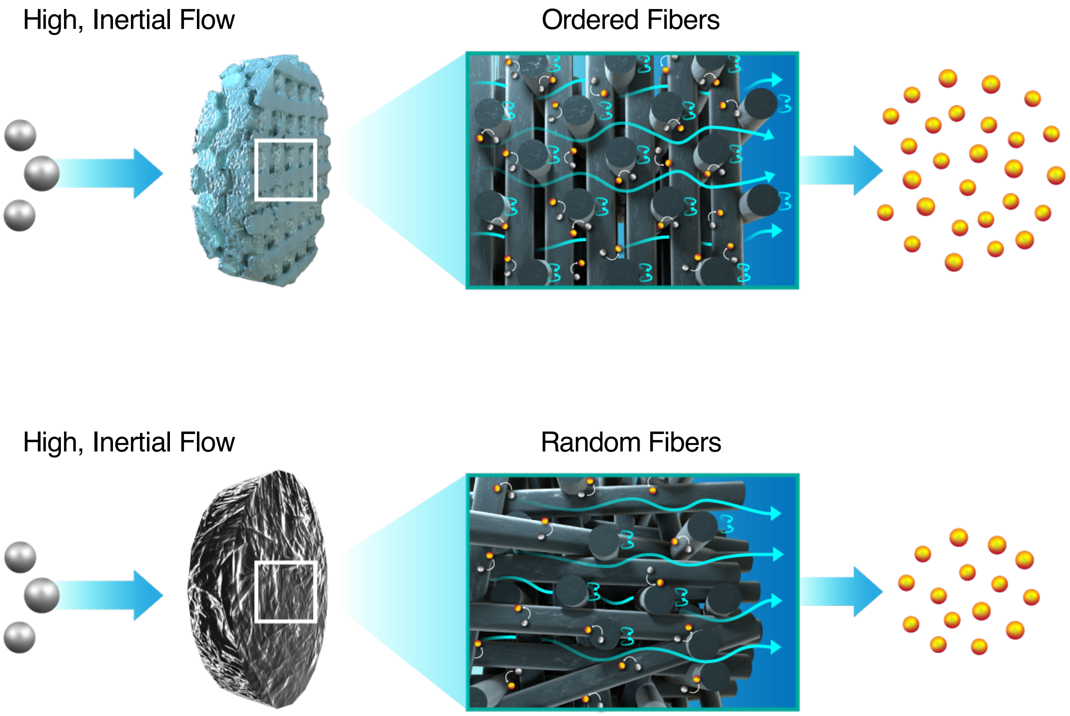

Fig. S4. Inertial flows are compared in ordered fiber lattices (top) and disordered fiber lattices (bottom). In this depiction, all fiber diameters are the same size and both flow-through electrodes are operated at the same flow rate. When the arrays are ordered and all fiber axes are orthogonal to incoming flow, the recirculating wake behind the fibers is maximized. In contrast, if the fibers are randomly oriented, only a subset of the fibers in the lattice will be oriented to enable to emergence of recirculating flow. Further, any flow along the fiber axis will diminish the emergence of recirculation.

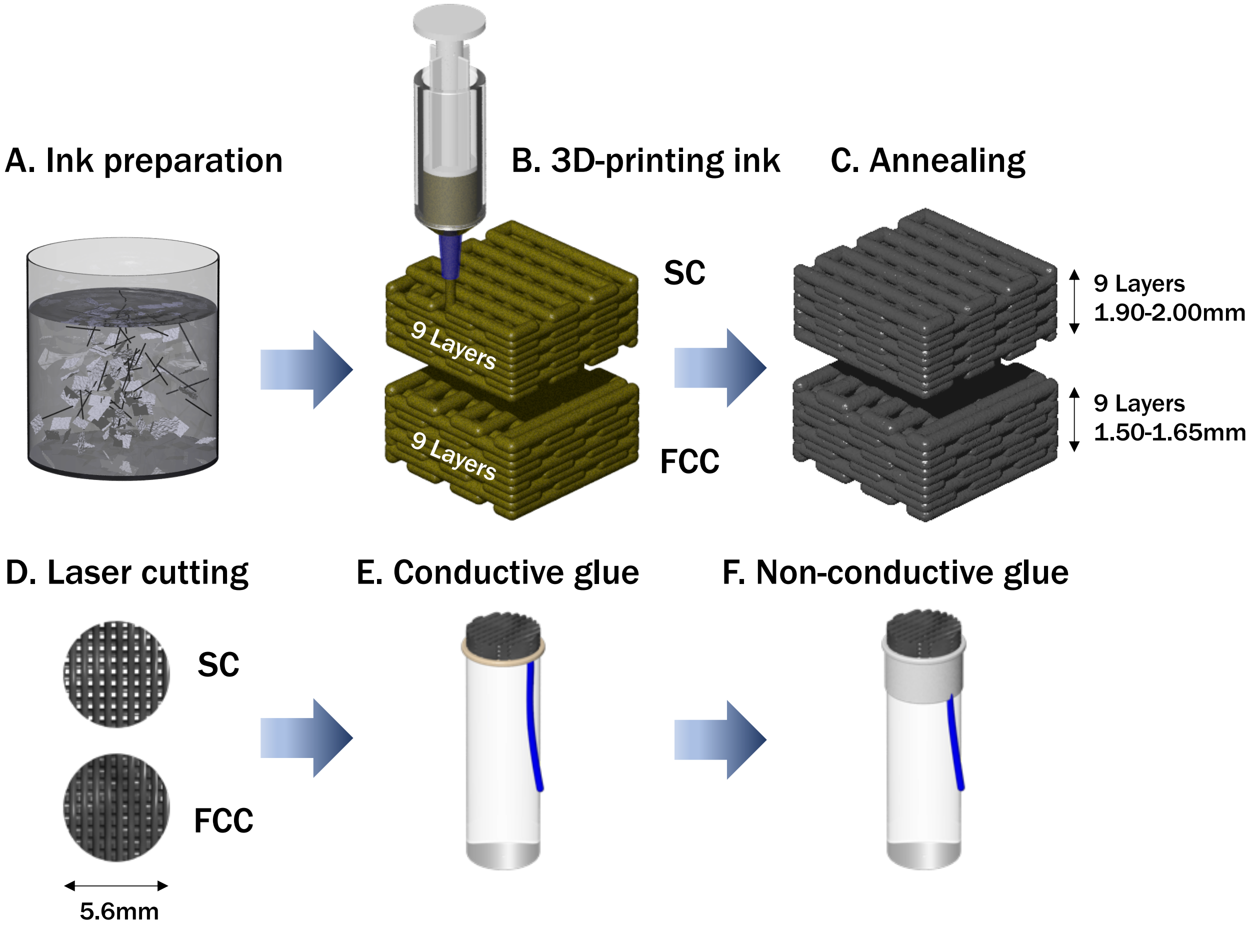

Fig. S5. Preparation of flow through 3D printed graphene electrodes.

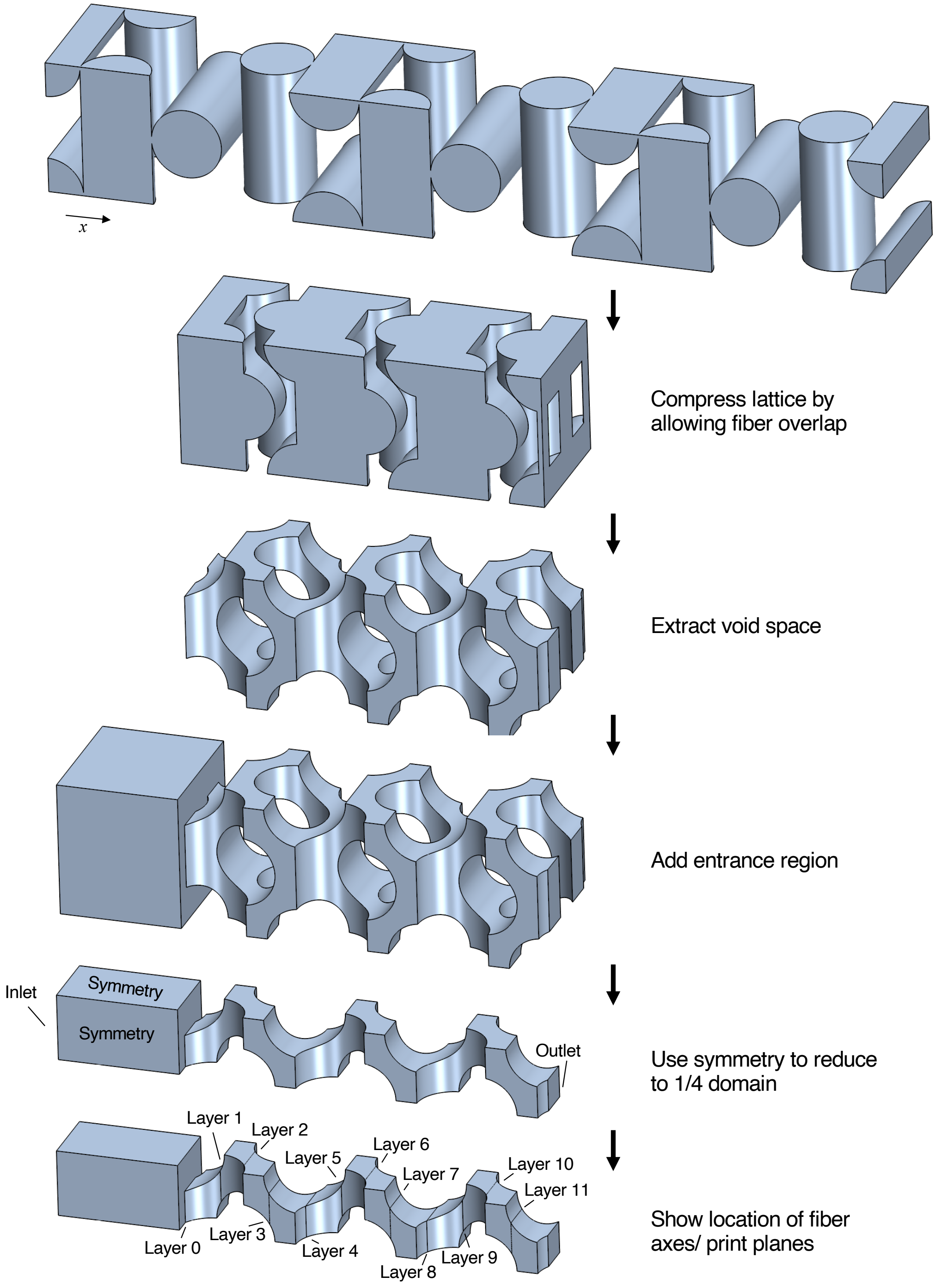

Fig. S6. Computational domain for simulation of fluid flow and species consumption in the FCC lattice. From the top, the typical FCC lattice is created by laying down fibers in successive layers in the x-direction, with each layer offset from the layer before. Because the inks slump, the lattice fibers overlap and the lattice is compressed. The void region is extracted from the compressed lattice and an entrance region is added to model the approach of the fluid to the lattice. Finally, symmetry is used to reduce this domain by 1/4. The boundary conditions and location of the print planes are labeled in the bottom two images. All curved surfaces (i.e., those not co-planar with a symmetry plane) are fiber surfaces.

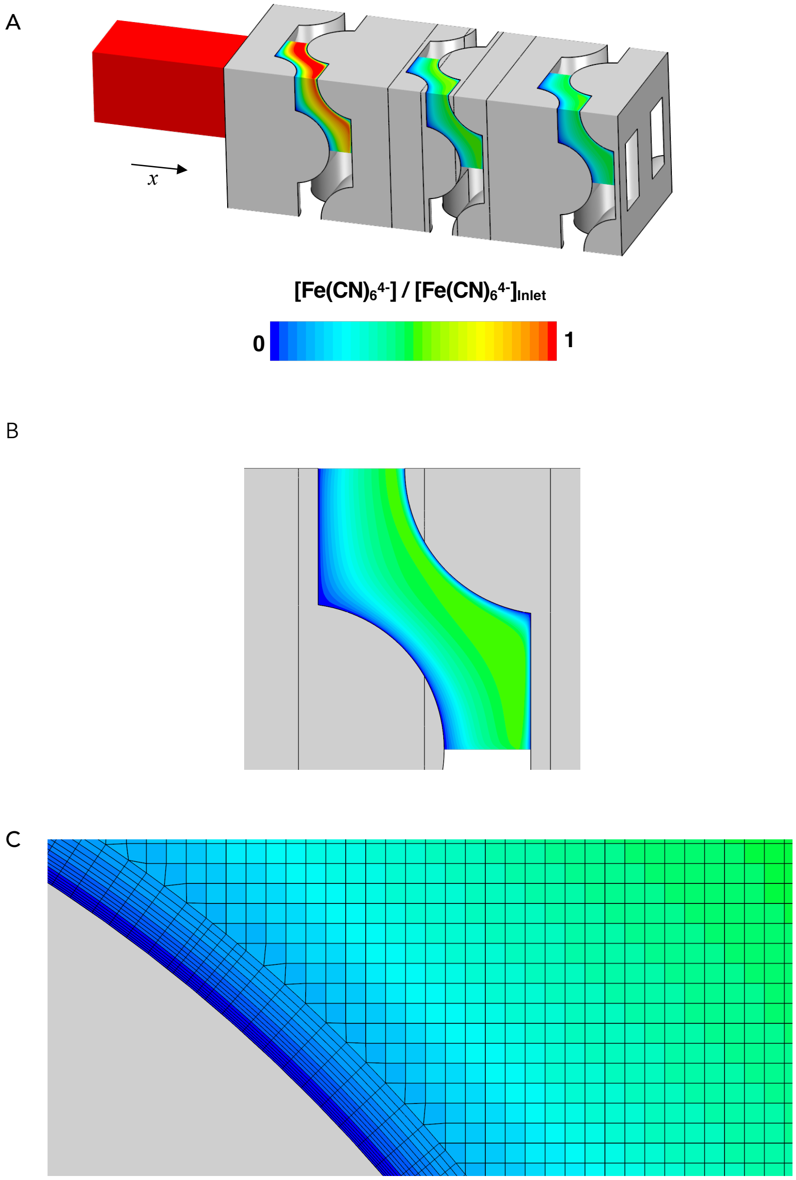

Fig. S7. (A) The fluid 1/4 domain is shown in context with the lattice (in gray). The fluid domain is colored by the normalized species concentration at Re_f = 1.8. This image is the same domain picture in main text Figure 1A but here we show the species concentration. (B) A zoom into the central portion of the lattice. (C) A further zoom with an overlay of the computational mesh. The edges of the faces of the mesh hexahedra are 2.5μm. A progressively growing prism layer is used to mesh the near-wall region of the fibers.

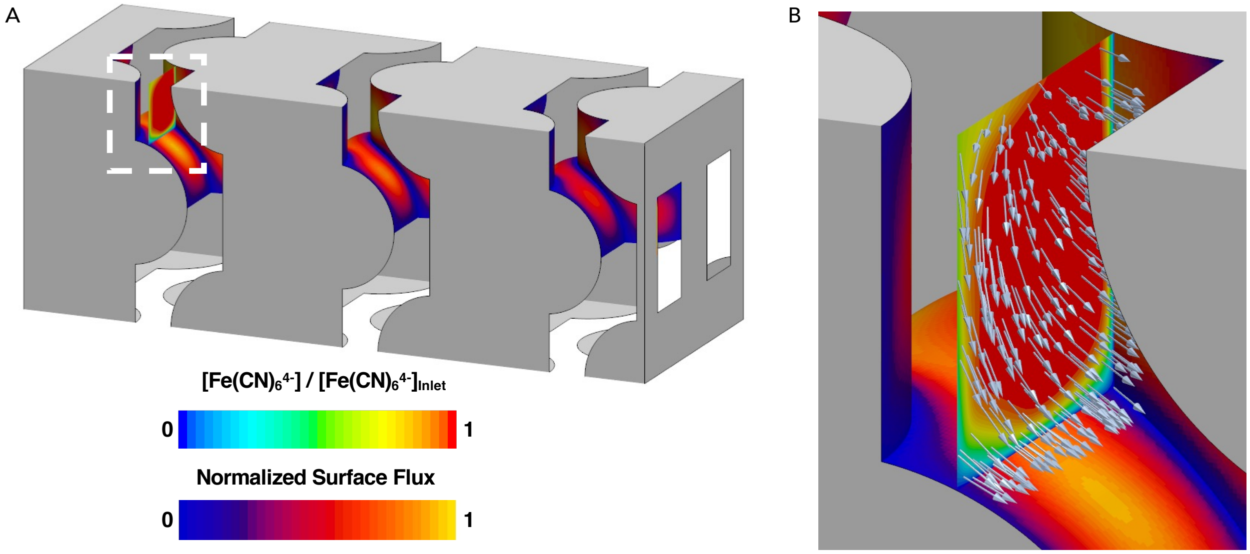

Fig. S8. Overview of the local km analysis. (A) Overview of the reactive surface flux on the fiber boundaries of the FCC lattice. An example plane for the determination of $k_m(x)$ is colored by the species concentration. The dashed region is enlarged in (B), and additionally we show velocity vectors with length scaled by the velocity magnitude. The flow average concentration, $\langle c \rangle_v$, is calculated by averaging the species concentration weighted by the velocity component normal to the plane (i.e., the x direction). The surface boundary flux is calculated by interpolating the reactive surface flux onto the line of intersection between the plane and the fiber surface. Simulation performed at $Re_f = 1.8$.

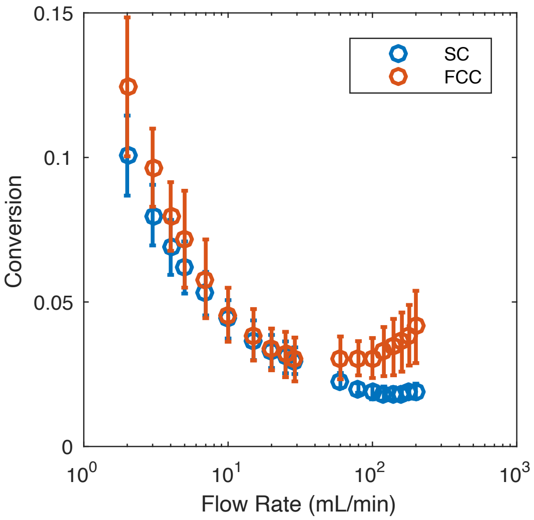

Fig. S9. Average reactant conversion. The conversion of the reactant defined as conversion = $(c_b - c_{outlet})/c_b$ = $I_{lim}/nFQc_b$ corresponding to the data in Fig. 2A of the main text.

References

1. SJ Gregg, KSW Sing, *Adsorption, Surface Area and Porosity.* (Academic Press), (1982).
2. J Newman, KE Thomas-Alyea, *Electrochemical Systems.* (John Wiley & Sons, Hoboken), (2012).
3. EJ Wilson, CJ Geankoplis, Liquid Mass Transfer at Very Low Reynolds Numbers in Packed Beds. *Ind. & Eng. Chem. Fundamentals* **5**, 9–14 (1966).
4. PS Fedkiw, J Newman, Mass-Transfer Coefficients in Packed Beds at Very Low Reynolds Numbers. *Int. J. Heat Mass Transf.* **25**, 935–943 (1982).
5. B Delanghe, S Tellier, M Astruc, Mass Transfer to a Carbon or Graphite Felt Electrode. *Electrochimica Acta* **35**, 1369–1376 (1990).
6. LF Arenas, C Ponce de León, FC Walsh, 3D-printed porous electrodes for advanced electrochemical flow reactors: A Ni/stainless steel electrode and its mass transport characteristics. *Electrochem. Commun.* **77**, 133–137 (2017) Publisher: Elsevier B.V.
7. TM Squires, MZ Bazant, Induced-charge electro-osmosis. *J. Fluid Mech.* **509**, 217–252 (2004).
8. AM Smith, AA Lee, S Perkin, The Electrostatic Screening Length in Concentrated Electrolytes Increases with Concentration. *J. Phys. Chem. Lett.* **7**, 2157–2163 (2016).